A New Robust Frontal Disturbance Index of the Oyashio Extension Sea Surface Temperature Front.

Richard J Hall[1], Arnaud Czaja[1], Gokhan Danabasoglu[2], Clara Deser[2], Claude Frankignoul[3,4], Young-Oh Kwon[3]

[1] Department of Physics, Imperial College, London
[2] National Center for Atmospheric Research, Boulder Colorado
[3] Woods Hole Oceanographic Institution, Woods Hole, Massachusetts
[4] LOCEAN, Sorbonne Université/IRD/CNRS/MNHN, Paris, France

Corresponding author
Richard J. Hall
Department of Physics
Imperial College
London SW7 2BW
rjhall@imperial.ac.uk

Abstract

The Oyashio Extension (OE) frontal zone in the Northwest Pacific Ocean is associated with strong gradients of sea-surface temperature (SST) and salinity. Like other frontal zones, the OE front enhances baroclinicity and anchors the storm tracks; thus, changes in its position and strength may impact atmospheric variability. North-south shifts in the OE front are often defined using the leading principal component for the latitude of the absolute maximum SST gradient in the Northwest Pacific (145-170°E)-the so-called Oyashio Extension Index (OEI). We show that the OEI is sensitive to the choice of SST dataset used in its construction, and that regressions of atmospheric fields onto the OEI also depend on the choice of SST datasets, leading to non-robust results. This sensitivity primarily stems from the fact that the longitudinal domain used to define the OEI includes a region with parallel or indistinct frontal zones in its central section (155-164°E), leading to divergent results across datasets. In particular, we advise against the use of ERA5 SST data for such analyses, as it is a clear outlier. To circumvent the robustness issue, we introduce a new index that considers the degree of continuity of the SST front across this central section - the Frontal Disturbance Index (FDI). We show that the FDI produces more robust results on the influence of the OE front on air-sea interactions and associated high-frequency storm-track metrics than the conventional OEI. There are significant asymmetric associations between the FDI and storm-track metrics dependent on the sign of the FDI.

Significance Statement

In this study we aim to understand how the choice of dataset may influence the interpretation of interactions between the ocean and the overlying atmosphere near sea-surface temperature (SST) fronts. We find that using different SST datasets affects the results, due to slight differences in the representation of the location of the maximum SST gradient. As a response to this we develop a new index which relates to the degree of disturbance of the SST front. This produces results that are more consistent across the different datasets. We also identify Some possible links between the frontal disturbance and the presence of ocean eddies. We advise that the sensitivity to dataset choice is given due consideration in regions near SST fronts.

1.Introduction

Oceanic western boundary currents (WBCs) transport significant quantities of heat eastwards and polewards in both the North Atlantic and Pacific Oceans. In the Atlantic the WBC is the Gulf Stream, while in the Pacific the configuration is different: to the south is the Kuroshio current, while to the north and forming part of the subpolar gyre, is the Oyashio current (Qiu, 2019). Both currents turn eastwards away from the coast of Japan and into the Pacific basin where they are known as the Kuroshio Extension (KE) and Oyashio Extension (OE; also sometimes referred to as the subarctic current or front), located at around 35°N and 41°N respectively (Kwon et al., 2010). The OE is associated with strong gradients of sea-surface temperature (SST) and salinity, whereas the KE is more clearly defined by a gradient in sea-surface height (SSH) (Qiu et al., 2017). These features are shown schematically in Figure 1. The region is very complex, with a number of diverging and converging currents between the two extensions (Kida et al., 2015; Yasuda, 2003)

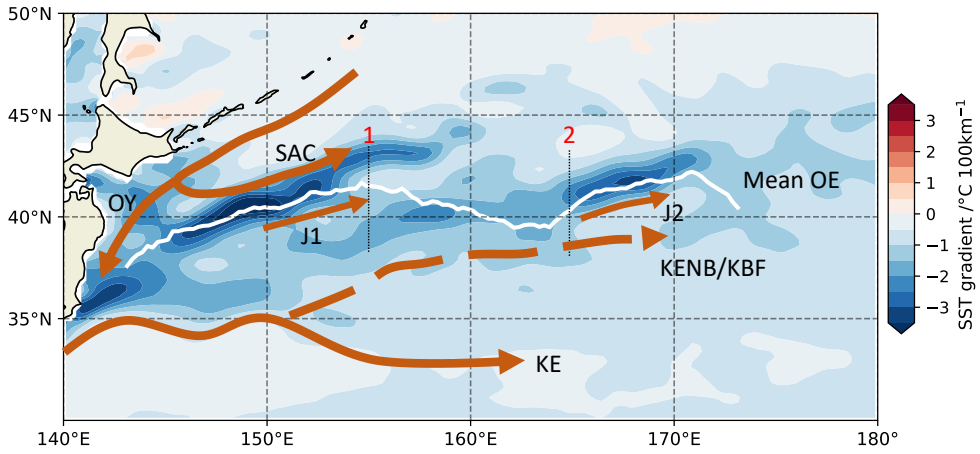

Figure 1. Schematic of the location of fronts referred to in the text. KE: Kuroshio Extension; KENB/KBF: Kuroshio Extension Northern Branch/Kuroshio Bifurcation Front; OY: Oyashio Current; SAC: Subarctic Current; OE: Oyashio Extension (143-173°E, shown in white); J1, J2: Isoguchi jets. Background field is the mean December-March (DJFM) SST gradient from the Reynold optimally interpolated (OI) SST dataset. (SST is not detrended). Meridional lines (1 and 2) mark the longitudinal segment within the OE used to calculate the Frontal Disturbance Index (FDI: 155-164°E). Data are not detrended.

The strong meridional gradients of SST in the OE region may act to enhance baroclinicity and anchor the storm track in the overlying atmosphere (Hoskins and Valdes, 1990; Nakamura et al., 2008) and have been the focus of numerous observational and modelling studies concerning air-sea interactions (Kwon et al., 2010; Frankignoul et al., 2011; Taguchi et al., 2012; Smirnov et al., 2015; Révelard et al., 2016; 2018). Air-sea heat fluxes associated with mesoscale air-sea

interaction are robust in the vicinity of WBCs (Seo et al., 2023). The SST signal from mesoscale processes such as eddies and SST fronts modify the surface turbulent heat and momentum fluxes and cause local responses in the marine atmospheric boundary layer (Small et al., 2008). This in turn drives a non-local response in the storm-track (e.g. Czaja et al., 2019; Seo et al., 2023). A poleward decrease in sensible heat flux across the frontal zone sustains the strong near-surface baroclinicity against the relaxing effect of strong poleward eddy heat transport (Sampe et al., 2010).

It is important to better understand the nature of SST variability and associated air-sea interactions along oceanic frontal zones, to improve the process level understanding of ocean-to-atmosphere feedbacks as well as the performance of model simulations. Crucial questions are the extent to which air-sea interactions over the OE region influence the wider atmospheric circulation, and how this depends on the sharpness of the SST gradient, location of the gradient and magnitude of the associated SST anomalies more generally (Small et al., 2019). Many modelling studies (e.g. Smirnov et al., 2015; Ma et al., 2017; Kuwano-Yoshida and Minobe, 2017; Yook et al., 2022) impose observed SST anomalies in the Kuroshio-Oyashio Extensions (KOE) region in an atmospheric model to investigate causal linkages. The atmospheric response may depend not only on the spatial resolution of the model, but also on that of the imposed SST anomalies. Only when the model has sufficient horizontal resolution can the full impact of mesoscale forcing by SST fronts on the storm track be correctly simulated (e.g. Smirnov et al., 2015; Ma et al., 2017).

To address these questions concerning air-sea interactions, there must be high confidence in determining the location and shifts in these SST frontal zones, and the nature of the associated SST anomalies. Frankignoul et al. (2011) developed an OE Index (OEI) based on the location of the maximum SST gradient in the OE region (145-170°E), which has been used in a number of subsequent studies (e.g. Kwon and Joyce, 2013; Smirnov et al., 2015; Qiu et al., 2017, Wu et al., 2018; Yao et al., 2018a,b). Frankignoul et al. (2011) identified that north-south shifts in the SST front were associated with large-scale atmospheric responses up to three months later. Subsequent work (Qiu et al., 2017) concluded that the western (145-153°E) and eastern (153-173°E) sections of the OEI were in fact uncorrelated on a synchronous basis over a range of different timescales, although lagged relationships did occur. The different sections of the front were driven by different physical mechanisms (Wu et al., 2018), and were associated with different SST anomaly patterns. It therefore makes sense to treat the variability of the two

sections of the front separately. Other studies identify SST frontal indices based on simple regional anomalies, although these are often applied to the general KOE region (e.g. 36-42°N, 140-171°E) and may provide different information about air-sea interactions that are not necessarily connected to shifts in SST fronts (e.g. Taguchi et al., 2012; Wills and Thompson, 2018).

The reliability of analyses of SST-front-driven air-sea interactions depends on the ability of SST datasets to accurately represent the SST front. New high-resolution gridded SST datasets are available, with horizontal resolutions commonly of 0.25° in latitude and longitude or higher. The credibility of these SST products depends upon the availability of observations and the gridding procedure used (Huang et al., 2021). Gridded SST datasets capture well large-scale modes of variability such as El-Nino-Southern Oscillation (ENSO) with high correlations between time series derived from different datasets (Yang et al., 2021). However, for assessing air-sea interactions over the WBCs and associated SST fronts, there is considerable variation between datasets and the sharpness of a front in the dataset is not necessarily proportional to the grid resolution used (Martin et al., 2012; Fiedler et al., 2019). These differences are related to distinctive retrieval and interpolation methods and interpolation grid-size, and bias-correction of input data (Yang et al., 2021).

We are therefore motivated to calculate the OEI for a range of SST datasets to determine first, their level of agreement and second, to identify whether the differences impact significantly on the interpretation of air-sea interactions. We also investigate whether any discrepancies in the OEI have any physical basis, and the significance of this for future studies. We find that the OEI interaction with atmospheric variables is dataset dependent. This leads us to develop a new index, the Frontal Disturbance Index (FDI), which, we think, is more robust to variations between datasets. The data used in the study are described in section 2, and methods are explained in section 3. Section 4 presents our results, and section 5 is a discussion and summary of our findings.

2.Data

In assessing air-sea interactions associated with SST fronts, reliable high-resolution SST datasets, which resolve mesoscale processes are required. One option is to obtain these from the newest generation of gridded observational datasets, with increased temporal and spatial resolution. The National Oceanic and Atmospheric Administration (NOAA) optimum-

interpolated (OI) SST version 2.1 dataset (Reynold et al., 2007; Banzon et al., 2016; Huang et al., 2020) is available at daily resolution on a 0.25° grid from 1981 to the present for the AVHRR-only product. The Operational Sea Surface Temperature and Sea Ice Analysis (OSTIA) dataset (Donlon et al., 2012; Good et al., 2020) is available from October 1981 onwards at a daily resolution on a 0.05° grid. In addition, we use the Group for High-Resolution SST Multi-Product Ensemble (GMPE, Martin et al., 2012; Fiedler et al., 2019) analysis for 1981 to 2016 at daily resolution on a 0.25° grid. The GMPE uses an ensemble of six high-resolution products (including OSTIA and OI; Fiedler et al., 2019) and takes the ensemble median value for each grid box, having regridded the data to a common grid. Details of the method are described by Martin et al. (2012). We also compare these products to the SSTs in the ERA5 reanalysis (Hersbach et al., 2020), available on a 0.25° grid with an hourly timestep from 1940 onwards. ERA5 uses Hadley Centre Ice and Sea Surface Temperature version 2.1.0 (HadISST2.1.0) for the period to 2007 (at 5-day and 1° resolutions; J.J. Kennedy, pers.comm), and OSTIA thereafter. It should be stressed that none of these datasets is independent, as they use many of the same satellite, and in-situ data sources; however they are selected as being representative of typical datasets that may be used in the analysis of air-sea interactions. We calculate monthly means of daily data for the common period January 1982 to December 2016, regridding to a common 0.25° grid. The OEI and FDI are calculated separately for each SST dataset (see section 3).

Atmospheric and surface flux variables (sea-level pressure (SLP), meridional wind, total precipitation, latent and sensible heat fluxes, vertical velocity (omega)) are obtained from the ERA5 reanalysis, to assess the impact of different OEI and FDI indices on storm-track variability. Sea-surface height (SSH) data are obtained by using the sea-level anomaly dataset from the Copernicus Marine Environment Monitoring Service (CMEMS). This is an altimeter satellite product available as gridded data at 0.25° and daily resolution, from 1993 (doi: 10.48670/moi-00148). For SSH we use the period 1993-2016, to ensure a common period with other datasets.

3. Methods

3.1 Definition of the Oyashio Extension Index (OEI)

Following Frankignoul et al. (2011), we calculate the OEI as the monthly standardised principal component (PC) monthly timeseries for the first empirical orthogonal function (EOF)

of the latitude of the absolute maximum meridional SST gradient for the September-to-April period, based on the monthly SST data. This period is chosen to avoid the summer season, because the summer SST gradient has different characteristics. We identify the latitude of the maximum SST gradient at each longitude over the OEI region at each timestep, but restrict the EOF calculation domain to the eastern part of the region (35-47°N, 153-173°E) following Qiu et al. (2017). We detrend the latitude of maximum SST gradients using a third order polynomial fit for the 1982-2016 period, and the mean seasonal cycle is removed by subtracting the climatological monthly means prior to the calculation of the EOF.

Based on the monthly OEIs calculated from each dataset following the above procedure, three versions of the OEI are calculated for the December-March seasonal window: 1) monthly; 2) seasonal mean; and 3) monthly intra-seasonal (anomalies from the seasonal mean for each year). These indices allow us to compare how similar the indices are at different temporal resolutions. We also calculate an extended monthly series from September to April. The OEIs from different datasets for each of these versions are compared by computing pair-wise correlation coefficients and a time series of average pair-wise differences (the "Difference index") is calculated for the September-April monthly timeseries.

3.2. Definition of the Frontal Disturbance Index (FDI)

The OE SST front is relatively weak and diffuse in the central portion of the domain (Fig. 1). To assess the extent to which the location of OE front departs from the climatology across this section, we compute a "Frontal Disturbance Index" (FDI) as follows. First, we calculate the detrended (third-order polynomial fit) standardised anomaly of the latitude of the SST front F as the latitude of the maximum SST gradient (ϕ) as a function of longitude (λ) and time ($t=1 \ldots N$) within 155-164°E:

$$F_{t,\lambda} = \frac{\phi_{t,\lambda} - \bar{\phi}_{\lambda}}{\sqrt{\frac{1}{N-1}\sum_{t=1}^{N}\left(\phi_{t,\lambda} - \bar{\phi}_{\lambda}\right)^2}} \quad (1)$$

where the overbar denotes time mean. Then, we find the root mean square deviation of these standardised anomalies with respect to longitude ($l=1 \ldots M$):

$$FDI_t = \sqrt{\frac{1}{M}\sum_{\lambda=1}^{M} {F_{t,\lambda}}^2} \quad (2)$$

Higher FDI values indicate a higher overall departure from the climatological time-mean. As constructed, the FDI captures both absolute departures from the time mean latitude, and also the extent to which the maximum SST gradient makes large latitudinal jumps between adjacent longitudes.

A schematic diagram of the FDI calculated for synthetic data is shown in Figure 2. For this example, the climatology has an FDI value of zero, the minimum possible. SST gradient locations are chosen to show that the FDI value is proportional to the absolute magnitude of the mean displacement from climatology, not the sign (red and blue lines have equal FDI values even though they are on opposite sides of the climatology). As distance from climatology increases, so does the FDI (gray line). While the green line is purely zonal in orientation, it has an FDI of 4.5 as it intersects climatology at an angle, with increasing differences further from the intersection. The two stepped lines are the reverse of each other. However, their FDIs are different, as with the orange line the step down is broadly aligned with climatology whereas in the purple line, as climatological values decrease eastwards, the step broadly increases in latitude. In the SST datasets analysed here, the range of FDI values is from around 0.3 to 1.9. We also calculate a mean FDI, which is the ensemble mean of the FDIs calculated for different datasets at a given monthly timestep. For use in asymmetric regression, we remove the climatological monthly mean FDI from the timeseries, thus the large negative FDI values indicate the frontal positions close to climatology.

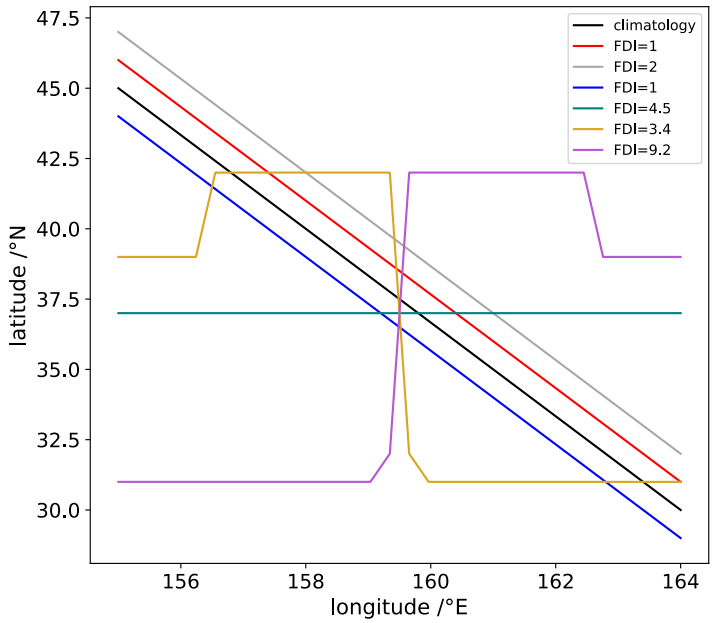

Figure 2. Diagram of synthetic data simulating different locations of maximum SST gradients, over the longitude and latitude range of the central section of the OE (155-164°E). The synthetic climatological maximum SST gradient is shown by the bold black line, and five different synthetic gradient locations are shown, together with the FDI value for each.

3.3. Other Calculations

To assess any physical mechanisms that might be linked to the FDI, we isolate oceanic mesoscale features (including coherent eddies) in the region 150-170°E, 30-50°N. We use a two-dimensional fast Fourier transform (FFT) spatial filter to isolate high and low wavenumbers in the SST data. We filter daily data, using a filter length-scale of 420km as a cutoff, (wave number equal to 0.0024 km^{-1}) to separate eddy length-scales from larger scales and then calculate the monthly standard deviation of the resulting data. The highpass filter isolates the mesoscale eddies, but produces a field with a lot of noise. To identify any large-scale patterns in the mesoscale eddies, we additionally apply a FFT lowpass spatial filter with the same cutoff as the highpass filter to the monthly standard deviation fields of the highpass data. For full details of the method used, see Sroka et al. (2022). For comparison we also calculate daily surface Eddy Kinetic Energy from the SSH data according to:

$$EKE = \frac{1}{2}\left(u_g'^2 + v_g'^2\right) = \frac{1}{2}\left[\left(-\frac{g}{f}\frac{\partial h'}{\partial y}\right)^2 + \left(\frac{g}{h}\frac{\partial h'}{\partial x}\right)^2\right], \quad (3)$$

where u'_g and v'_g are the zonal and meridional components of the geostrophic current anomaly respectively, f is the Coriolis parameter, g is the gravitational acceleration, h' are the SSH

anomalies and y and x are distances along the latitudinal and longitudinal directions respectively.

We calculate the monthly standard deviation of 8-day highpass-filtered daily data of surface turbulent heat flux (THF, the sum of sensible and latent heat fluxes) and 500hPa vertical velocity (omega) by applying a 4-point highpass Butterworth filter to the daily data, to isolate variability at the synoptic timescale. These fields can give an indication of storm-track activity, increased variance being associated with passage of low-pressure systems, where both enhanced positive and negative heat fluxes and vertical velocity can occur in different locations within the same system, associated with warm and cold sectors and fronts. We also calculate indicators of surface storm-tracks, using an alternative highpass filtering approach involving daily differencing (Wallace, 1998). We apply this to 850hPa meridional wind and total precipitation. In addition, the Eady Growth Rate (EGR) at 800hPa is calculated according to:

$$EGR = -0.31 \frac{g}{N\theta_o}\frac{\partial\theta}{\partial y} \quad (4)$$

where N is buoyancy frequency, θ is potential temperature and θ_o is the climatological monthly mean temperature (e.g., Small et al. 2014). The EGR is an important measure for identifying baroclinic eddy development (e.g. Hoskins and Valdes, 1990).

We identify large-scale air sea interactions associated with the OEI and FDI by regressing the different atmospheric variables including storm-track metrics from ERA5 (section 2) on the monthly timeseries. We use both conventional symmetric linear regression and asymmetric regression to accommodate potential non-linear associations with respect to the sign of the index (e.g. Révelard et al., 2016). The asymmetric regression method is described in detail in Frankignoul and Kwon (2022). Negative and positive values of the index (recall the FDI is adjusted by removal of the climatological mean, creating positive and negative values) are regressed separately against the relevant time steps of the cubic-detrended anomaly field, having first removed the time mean for negative and positive index values, separately, from each set of data to provide an unbiased estimate. Statistical significance for regressions is determined using the Wald test (similar to the Student's t-test; Wald, 1943) and we present results for two levels of significance ($p<0.1$, $p<0.2$). We apply the False Discovery Rate (FDR; Benjamini and Hochberg, 1996; Wilks, 2015) to compensate for spatial autocorrelation and multiple testing.

4.Results.

4.1 The Sensitivity of the OEI to Choice of Dataset.

Correlations between the OEIs show considerable variation between dataset pairs and depend on the temporal window and resolution used (Table 1).

correlation	SONDJFMA separate months	DJFM separate months	DJFM Seasonal mean	DJFM subseasonal anomalies
ERA5 vs. OI	0.72	0.62	0.69	0.49
ERA5 vs. GMPE	0.71	0.61	0.71	0.46
ERA5 vs. OSTIA	0.71	0.57	0.75	0.24
OI vs. GMPE	0.81	0.78	0.88	0.58
OI vs. OSTIA	0.80	0.72	0.77	0.53
GMPE vs.OSTIA	0.78	0.72	0.86	0.41

Table 1. Pearson correlations between the PC-based OEI timeseries for different SST datasets, and for different temporal resolutions. All correlations are calculated for 1982-2016. All correlations are significant ($p<0.05$).

The correlations are higher for the September-April monthly resolution timeseries than for the extended winter (DJFM) monthly series, indicating weaker correlations in the winter months. Correlations for DJFM seasonal means are quite high (0.69-0.88), while those for subseasonal anomalies are much lower (0.24-0.58). The correlations for time series of separate DJFM months lie somewhere in between. Correlations with ERA5 and other datasets are generally lower than those between other dataset pairs.

The September-April (SONDJFMA) OEI with monthly resolution shows good agreement across datasets at multiannual timescales (Figure 3a), while the Difference Index shows that there can be considerable disagreements on monthly timescales (Figure 3b). Over the September to April window, a seasonal cycle in correlations between ERA5 and the other datasets is evident (Figure 3c) with lower correlations in the winter months (generally February and March). The lower ERA5 correlations in February and March are also present in the subseasonal anomalies, although here the correlations are even lower, with increased noise in the datasets at subseasonal timescales (Figure 3d). These correlation statistics suggest that the OEI may be most suitable for use with seasonal means for calculating interannual variability.

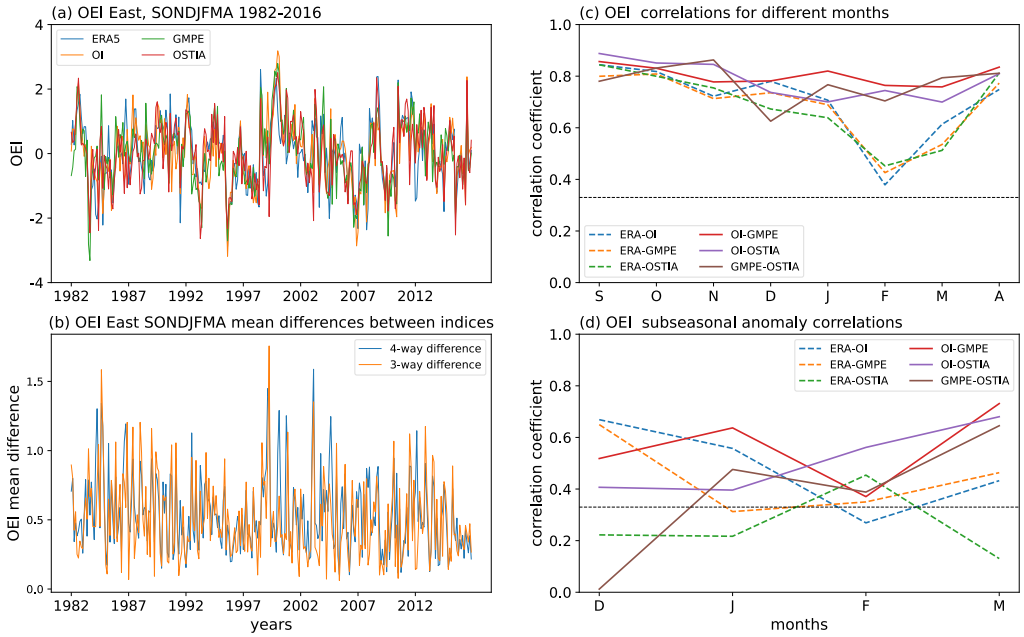

Figure 3 (a). The OEIs (eastern section, 153-173°E) for September to April with monthly resolution based on the 4 different SST datasets, and (b) the mean absolute difference between the indices, calculated between all indices (4-dataset difference) and without ERA5 (3-dataset difference). (c) Interannual correlations between OEIs for each month in the window September - April based on different pairs of SST datasets. (d) As in (c) but for the subseasonal anomalies in DJFM. In c) and d) correlations between ERA5 and other datasets are shown as dashed lines and the horizontal dashed lines denote the significance threshold for $p<0.1$.

When atmospheric and SST fields are regressed on these different OEIs, the results are inconsistent across the datasets, leading to concerns regarding interpretation when a single dataset is used (Figure S1). When OEI timeseries and SST datasets are swapped, so that for example the OI SST is regressed on the ERA5 OEI, the same spatial patterns of regression coefficients are obtained as that when regressing the ERA5 SST on the ERA5 OEI. This suggests that inconsistencies arise from the OEIs.

From the results shown in Figure 3, ERA5 seems to be an outlier in that it disagrees with other SST datasets considered. Thus, we do not consider this SST product further in the subsequent analysis.

4.2 Reasons for OEI Discrepancies

Here we investigate the differences in the OEI across datasets to identify their origin. Our focus is on the spatial structure of SST gradients within the OE region.

The SST gradient pattern in the OE region is complex. As an example, the February-mean SST gradient pattern for the OSTIA dataset is shown in Figure 4a. The region does not contain a single continuous front: there are parallel fronts, single well-defined fronts and regions where the front is poorly defined. Other datasets have very similar patterns (Figure S2) and those for other months are qualitatively similar (not shown).

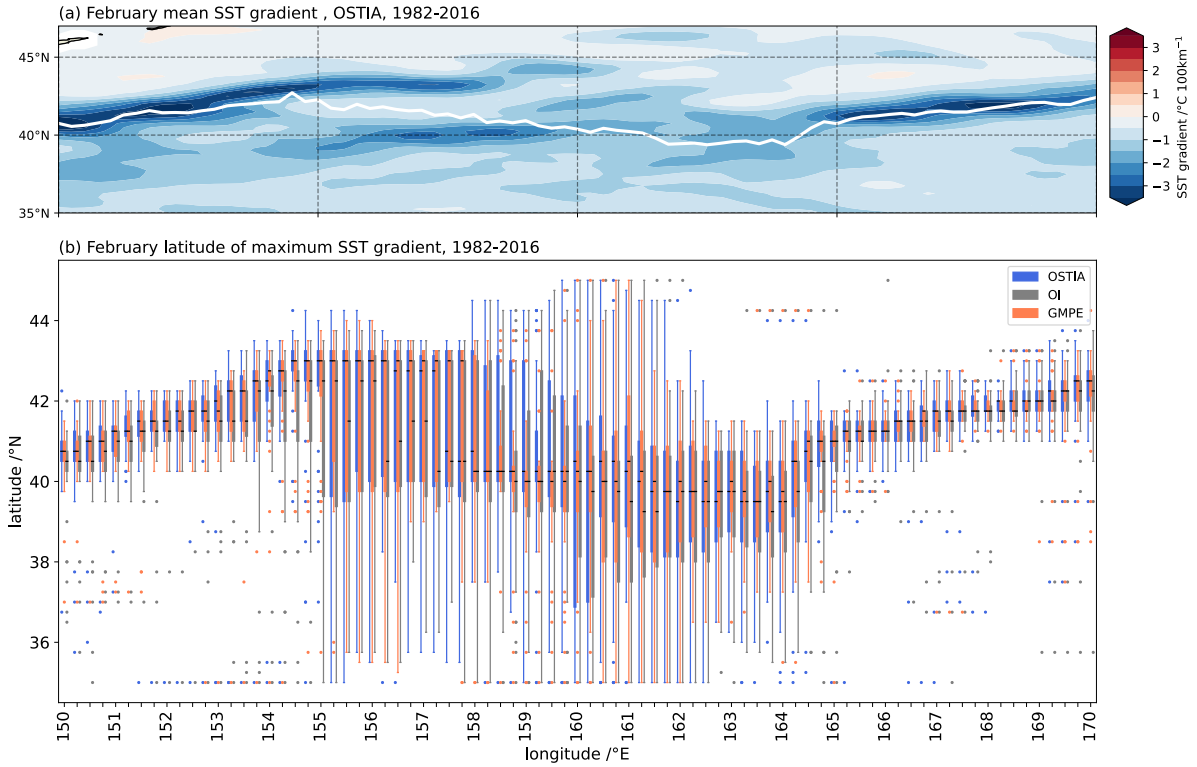

Figure 4. (a) Spatial pattern of the February mean SST gradient from OSTIA for 1982-2016. White line shows the February climatological absolute maximum SST gradient. (b) Box and whisker plots showing the February latitudinal distribution of the maximum poleward absolute SST gradient at each longitude, for each dataset for 1982-2016 (OSTIA in blue, OI in gray and GMPE in orange). The central box at each longitude shows the interquartile range (IQR), the horizontal black line indicates the median. The whiskers extend from each box by 1.5 times the IQR and dots indicate values that occur outside these ranges.

The latitudinal occurrences of absolute maximum poleward SST gradients shown for February in Figure 4b illustrate these distinct regions. Within 150-155°E and 165-170°E there are strong, well-defined SST gradients. These clearly defined SST fronts to the west and east correspond to the locations of the Isoguchi jets (Isoguchi et al., 2006; Kida et al., 2015; J1 and J2 in Figure 1). These quasi-stationary geostrophic jets transport warm water polewards. This explains their consistent representation amongst the datasets and the relatively narrow interquartile ranges

(IQR) in Figure 4b. However, within 155-165°E, the pattern of SST gradients is more complex. Two parallel SST gradient fronts are evident from 155-160°E (one near 40°N, and the other near 43°N (Figures 4a and S2). The broad IQRs on the boxplots here indicate sampling of the maximum SST gradient from both regions of strong SST gradients (figure 4b), with datasets showing different preferred latitudes at different longitudes and times. While OSTIA and GMPE show a skewed distribution with more frequent sampling of the northern front, the median value for OI is located further south, particularly between 156-157°E, indicating that the maximum SST gradient occurs more frequently along the more southern SST gradient region in OI. At around 159°E, OSTIA has a much wider IQR than either OI or GMPE. Between 160-164°E there is a more diffuse front, with fragmented sections of stronger and weaker gradients. In February this zone of weak overall gradients is broadest latitudinally and may contribute to the low correlations in OEI timeseries in February (Figure 3c,d). Some of the differences between the OEIs arise from the central section: either slight differences in the representations of the relative strengths of the parallel fronts in its western half means that different latitudes are selected by the datasets, or over the diffuse, shallow front in the eastern half, small differences in gradient strength could result in large latitudinal discrepancies between datasets. Other months are qualitatively similar and display the same regions of discrepancies (not shown).

4.3 OE Variability and Frontal disturbance for 155-164°E

We now examine the central section of the OE SST front, using the FDI calculated over 155-164°E. This longitude range comprises just under half the length of the OE used to calculate the Eastern OEI (153-173°E). Recall that a high FDI indicates the OE front has a large departure from climatology, whereas the smaller the value, the closer the front is to climatology. The correlations between the GMPE and other FDI timeseries from different datasets, at different temporal resolutions, are not as strong as those obtained from the OEI, except for the DJFM subseasonal anomalies which are of similar magnitude. (Table 2, compared with Table 1). This may be a consequence of the methodology used in constructing the GMPE: selection of the median value from an ensemble at each grid point may not reflect the actual disturbance of the front. Correlations between the OI and OSTIA FDI are of similar magnitude to those of the OEI (greater in the case of subseasonal anomalies) and the correlations for individual months are the lowest in December-April (Figure S3).

correlation	SONDJFMA separate months	DJFM separate months	DJFM Seasonal mean	DJFM subseasonal anomalies
OI-GMPE	0.61	0.55	0.56	0.55
OI-OSTIA	0.76	0.69	0.67	0.55
GMPE-OSTIA	0.64	0.62	0.77	0.40

Table 2. Pearson correlations between the FDI timeseries for 155-164°E for different datasets and timesteps. All correlations are over the 1982-2016 period and all correlations are significant ($p<0.05$).

During September-April at monthly resolution, the FDI shows no significant ($p<0.1$) correlations with the OEI in any of the datasets. However, if the OEI and FDI are partitioned based on the negative and positive OEI phases a different picture emerges. The positive phases of the OEI are positively correlated (OI: 0.54; GMPE: 0.59; OSTIA: 0.52) with the FDI, whereas for the negative phases of the OEI, they are negatively correlated (OI: -0.47; GMPE: -0.54; OSTIA: -0.50) with the FDI. These results explain why the correlations are negligible when the full timeseries are considered, but also identify a moderate association between poleward shifts (OEI) and increased frontal disturbance (FDI) in the positive phase. When the OEI is negative, a southward shift is also associated with a more disturbed front (a more positive FDI). The FDI increases as the OE front moves away from the climatological location in either direction. The relationship between the OEI and FDI is summarised in Figure 5.

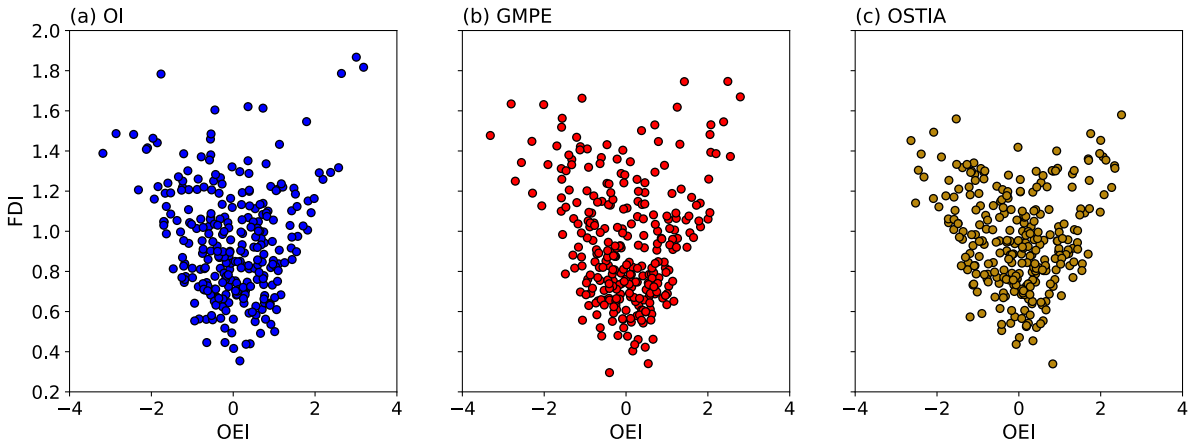

Figure 5. Scatterplots of the monthly OEI against monthly FDI for September-April, for (a) OI) (b) GMPE and (c) OSTIA datasets, 1982-2016.

In February, of the 12 years with the lowest OEI Difference Index, six have a low FDI, and one has a high FDI. Conversely, when the OEI Difference Index in February is high, three of the 12 years have a low FDI and seven have a high FDI. This makes sense as a broken, less

well-defined front may well be detected more ambiguously in different datasets. Additional contributions to the Difference Index come from the more well-defined regions of the front, where differences still occur for each timestep.

Using the OI SST dataset and considering the SST gradients in February as an example, the FDI is high in the year 1991 (1.25) and low in 1995 (0.42) (Figure 6). In Figure 6a, the climatological mean for the locations of the maximum SST gradients (black curve) does not coincide with the climatological February-mean for the SST gradient field (shading). In the west it lies between the two regions of strong poleward SST gradients, a consequence of the average location reflecting fluctuations in the relative strength of the northern and southern SST fronts. In 1991, large sections of the maximum SST gradient are located well to the north and south of the climatology (Figure 6b), with the maximum around 35°N likely associated with the KE. Such a large overall disturbance results in a high FDI in 1991. In contrast, in 1995, the maximum SST gradients are close to but either side of the climatological values, with an overall more zonal location and a low FDI.

A summary of the latitudinal distributions (density) of the absolute maximum SST gradients for all Februarys (Figure 6d-f) shows that when the FDI is high (red), the distribution has a greater spread, with higher and lower latitude values in the tails; whereas for low FDI years (blue), the distribution has increased frequency around 40°N. High FDI months sample the maximum SST gradients from higher or lower latitudes more frequently, with fewer occurrences at around 40°N.

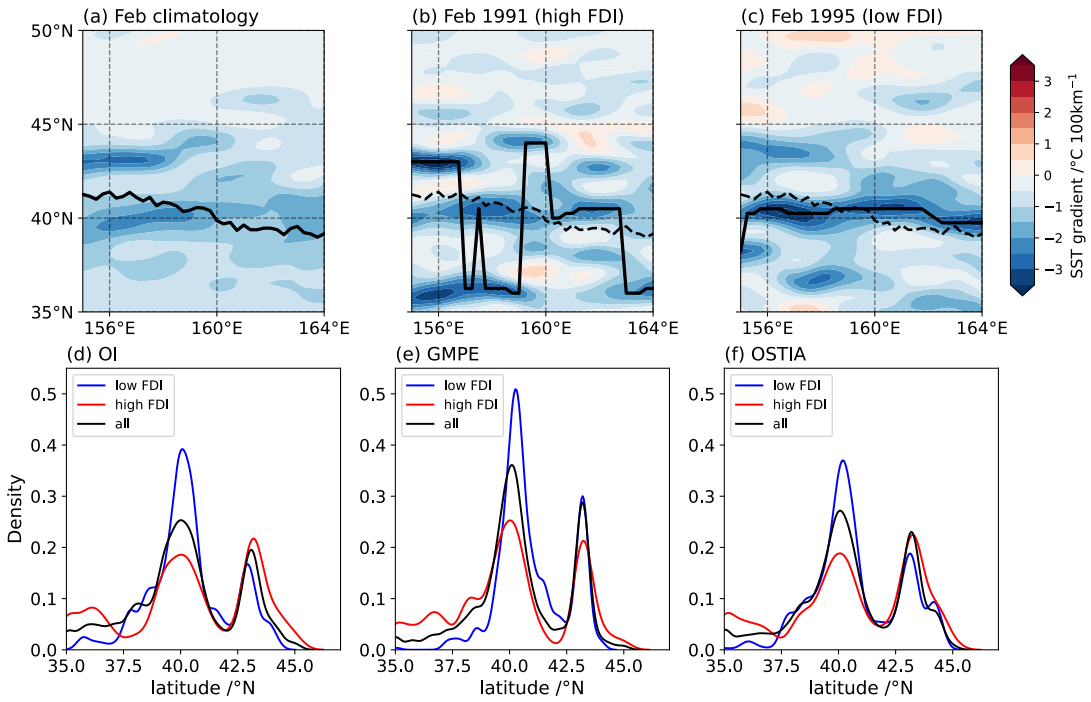

Figure 6. February-mean poleward SST gradient (color shading, °C per 100km) for (a) February climatology 1982-2016, (b) February 1991 (a high FDI case) and (c) February 1995 (a low FDI case) from the OI SST dataset. In (a), the locations of the maximum absolute SST gradients are shown with a black solid line which is drawn as black dashed lines in (b) and (c). Data are not detrended in (a–c). (d-f) Kernel density estimates of the distribution for latitudes of the February maximum absolute SST gradients, at each longitude and for each February in 1982-2016 for (d), OI, (e) GMPE and (f) OSTIA. Blue (red) curves show the third of months with the lowest (highest) FDI, and black curve is for all the February months.

4.4 Physical Factors Associated with the FDI.

The FDI is moderately associated with the magnitude of the poleward SST gradient averaged over 39-41°N, 155-164°E. Specifically, correlations between the FDI and SST gradient are 0.43(OI), 0.30 (GMPE) and 0.38 (OSTIA), based on monthly data during 1982-2016). All these values are highly significant ($p < 0.01$) and indicate that a stronger (more negative) poleward temperature gradient at 40°N is associated with a lower FDI, closer to climatology. This implies a stronger SST gradient at this latitude is more likely to be selected as part of the OE front defined along the maximum absolute SST gradient. Figure 6 provides an example of this: in the high FDI case (Figure 6b), there are regions of stronger (than climatology) positive poleward SST gradients to the north and south of 40°N, whereas in the low FDI case (Figure 6c) the gradients along 40°N are the strongest in the domain. The probability density functions in Figure 6d,e,f reinforce this. There is a clear increase in occurrences of maximum SST gradients at around 40°N for low FDI months (blue lines), while for high FDI years, this frequency decreases, with increased frequency particularly at lower latitude (35-37°N, red

lines, in the KE region). There is a secondary frequency peak at around 43°N, where changes in frequency are dependent on dataset. The magnitude of the SST gradient at around 40°N explains only a part of the FDI, as it is likely to be a result of interactions between a range of variables related to local SST, SST gradients and SSH gradients, some of which may be non-linear.

We now consider whether mesoscale oceanic eddy activity has any influence on the FDI. The amplitude of mesoscale eddy activity is calculated from the monthly standard deviation of daily OI SST data that have been highpass-filtered by application of a spatial FFT filter (Section 3.3; Figure 7). There is high mesoscale eddy activity in the region between the KE and OE (Figure 7a) (~35-41°N). In addition, there is increased eddy activity along the two quasi-stationary regions of strong SST gradient associated with the OE Front (150-160°E, 40-44°N, and 165-170°E, 40-43°N).

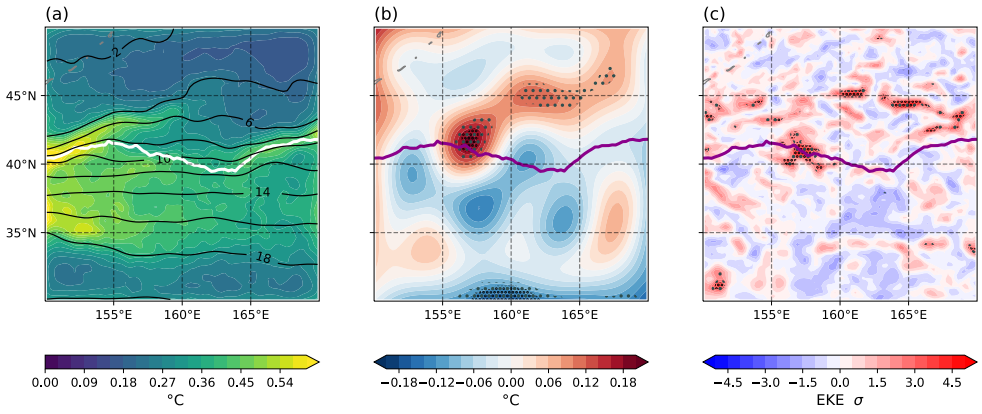

Figure 7. (a) OI SST monthly standard deviation of spatially high-pass filtered daily data averaged over DJFM, 1982-2016. Black contours show the DJFM mean SST. (b) Monthly standard deviation of daily spatially highpass filtered SST, with additional lowpass filter applied to the monthly standard deviations prior to regression, regressed against the OI FDI (for positive FDI months only). (c) monthly mean Eddy Kinetic Energy standardised anomalies regressed against the average FDI (positive regression only). Stippling indicates significance at $p<0.1$ (fine black) and $p<0.2$ (coarse gray) after the application of the False Discovery Rate. The monthly SST data are detrended prior to regression. The DJFM mean location of the OE is shown in white in (a) and magenta in (b) and (c).

The FFT-filtered OI SST fields regressed onto the FDI for December-March results in significant increased mesoscale eddy energy in positive regression (Figure 7b) to the north of the climatological SST. The additional lowpass filtering cleans up the very noisy highpass-filtered fields. A similar pattern is observed using OSTIA data, although the field is noisier and results are not significant (not shown). However, if the regressions are repeated for December-January or January-February, significance is found using both OI and OSTIA (not shown; note

that we do not use GMPE for these results as the median method of calculation used for creating GMPE may potentially have a smoothing effect on mesoscale features). A high FDI indicative of a more disturbed maximum SST gradient, is associated with increased eddy activity to the north. To confirm the association between mesoscale eddy activity to the north of the Oyashio SST front and the FDI, we regress the eddy kinetic energy (EKE) monthly-mean standardised anomalies against the average FDI (Figure 7c). In agreement with the results derived from spatial highpass-filtered SST, the EKE from SSH indicates increased eddy activity to the north of the SST front for a positive FDI. If the monthly standard deviation of standardised EKE anomalies is regressed against the average FDI, a similar pattern emerges (not shown) suggesting a shift in both the mean and spread of EKE with an increased FDI.

There is evidence of significant oceanic mesoscale eddy activity leading the FDI by one month (not shown), further suggesting the mesoscale eddy activity is influencing the FDI. While the FDI shows an association with SST mesoscale eddy activity, there is no significant association with local unfiltered SST variability (not shown).

4.5 Impacts of Changes in Frontal Continuity

We now address whether the variability of the FDI is manifested in atmospheric fields over a North Pacific domain defined by the region between 130-240°E and 30-65°N by regressing the various storm-track metrics (highpass-filtered turbulent heat flux (THF) and 500hPa omega; daily-differenced 850hPa meridional wind and total precipitation and 800hPa EGR) and SLP against the FDI. We compare the results with analogous regressions based on the more familiar OEI. We primarily examine significant regressions at one-month lag between the respective FDI and OEI in January and February (JF) and the February and March (FM) atmospheric fields, at monthly resolution. This time lag is chosen to capture the influence of the changes in frontal disturbance or OE shift on the atmosphere, avoiding atmospheric influences on the ocean which dominate at zero lag. Significant changes can also be observed at longer lags (not shown); however we do not aim to be exhaustive here, focussing instead on the novel result that the frontal disturbance of the central section of the OE is associated with significant changes in atmospheric variables at one-month lag. We focus on a small number of metrics below for clarity, and also average the indices across the different datasets, to reduce noise.

Symmetric and asymmetric regression results are summarised in Table 3, with statistical significance at $p<0.1$ and $p<0.2$ indicated by dark and light blue shading, respectively. Recall

that for these regressions we remove the climatological mean FDI to create positive and negative values. It is notable that for the FDI, there are no significant negative results for the individual datasets, (i.e. when the fronts are closer to their climatological mean position). Similarly for the OEI, significances for positive regressions, when the front shifts to the north, are much more frequent than for negative regressions. In addition, for the FDI, significance is found for positive regressions of SST mesoscale eddy activity (Figure 7) and the storm-track metrics (Figure 9; Table 3) against the FDI, suggesting a possible causal link between SST mesoscale eddies and storm-track metrics a month later.

(a)	**February-March atmospheric field**																	
FDI dataset JF	**THF SD highpass**			**500hPa omega SD highpass**			**850hPa v wind differences SD**			**Total Precip. differences SD**			**800hPa Eady Growth Rate**			**SLP**		
	+	-	s	+	-	s	+	-	s	+	-	s	+	-	s	+	-	s
OI																		
GMPE																		
OSTIA																		
MEAN																		
Agreement score	0	0	3	4	0	0	5	0	0	3	0	0	4	0	0	4	0	3

(b)	**February-March atmospheric field**																	
OEI dataset JF	**THF SD highpass**			**500hPa omega SD highpass**			**850hPa v wind differences SD**			**Total Precip. differences SD**			**800hPa Eady Growth Rate**			**SLP**		
	+	-	s	+	-	s	+	-	s	+	-	s	+	-	s	+	-	s
OI																		
GMPE																		
OSTIA																		
MEAN																		
Agreement score	0	0	0	2	0	0	2	0	0	4	0	0	0	0	0	5	0	0

Table 3 Table showing where significant regression coefficients occur in regression maps of (a) the JF FDI and (b) the JF OEI, for indices derived from each dataset against atmospheric and storm-track variables. +, - and s denote positive, negative and symmetric regression cases respectively. Light blue indicates that the regression map shows regions of significance at $p<0.2$, and dark blue indicates that there is significance at $p<0.1$, after application of the False Discovery Rate. SD = monthly standard deviation of daily highpass-filtered or daily-differenced data.

The FDI shows closer agreement than the OEI for the significant regressions of storm-track fields against different dataset indices. For example, all three datasets show significant positive

556 regressions of the meridional wind differences against the FDI. However, for the OEI there is
557 less agreement between the different dataset indices. A simple agreement score is employed to
558 quantify this. If two of the three dataset indices (the mean indices are not included) agree in
559 showing regions of significance, points are awarded, two for $p<0.1$, one for $p<0.2$. Based on
560 the agreement score, there is a moderate to high level of agreement between the FDI regressions
561 for the different dataset indices in positive regressions which suggests that these features are
562 robust. For the OEI, there are fewer instances of agreement in significance, and much of the
563 agreement is at a lower significance threshold. When considering SLP, indicative of impacts
564 on large-scale atmospheric variability, both the OEI and FDI show good agreement between
565 the different datasets for the positive phase regression, while disagreeing on the negative and
566 symmetric regressions.
567
568 Next we present the results from the OEI regressions using the mean OEI averaged over three
569 datasets (Figure 8). All significant regressions occur for the positive regression case, when the
570 OE is shifted northwards. A significant ($p<0.1$) low sea-level pressure (SLP) monopole is
571 centred over the Aleutian Islands (dashed magenta contours in Figure 8), and significant
572 regression coefficients for the storm-track metrics occur consistently on the southern flank of
573 the low-pressure anomalies: a northward shift of the OE is associated one month later with
574 increases in the standard deviation of meridional wind and total precipitation daily differences,
575 and an increase in 800hPa EGR, mainly between 180-140°W (Figure 8d). This indicates an
576 eastward extension of storm-track activity downstream of the OE, with the OE leading by one
577 month. The daily-differenced parameters are associated with the transit of low-pressure
578 systems along the storm-track. The increased variability reflects the increased passage of fronts
579 or stronger storms, which are accompanied by changes in wind direction; and the warm and
580 cold sectors, where rainfall and meridional winds are more vigorous and also more changeable.
581 Significant increases in omega at 500hPa are located on the northern flank of the climatological
582 storm-track (figure 8a). Descending cold air (positive omega) is associated with the cold sector
583 behind the cold front, and ascending warm air (negative omega) is linked to the warm front
584 ahead of the warm sector, which will combine to increase variability of omega when storm-
585 track activity increases.

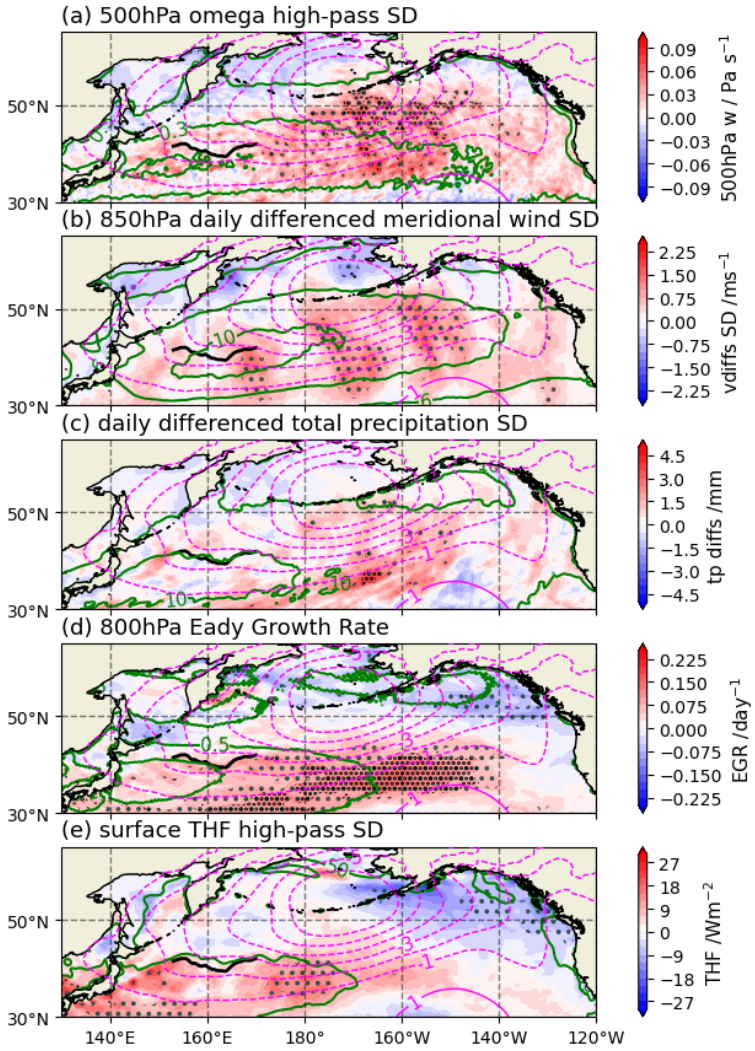

586

587 **Figure 8.** Asymmetric (positive) regression on the dataset averaged OEI, 153-173°E for JF,
588 for various FM atmospheric fields related to storm tracks. Maps are only shown where there
589 are significant regression coefficients ($p<0.2$), after the FDR is applied. Shading shows
590 significance at $p<0.2$ (coarse gray) or $p<0.1$(fine black). The contours of the SLP regression
591 coefficients are shown in magenta, dotted for negative values and the zero contour is omitted
592 (contour interval 1hPa). The solid black line shows the mean position of the OE front. Green
593 contours show the climatological mean values of the respective atmospheric field. Contour
594 intervals: 0.1 Pa s^{-1} (highpass-filtered omega SD); 2ms^{-1} (v wind differences); 5mm (total
595 precipitation differences); 0.25 day^{-1} (EGR); 50W m^{-2} (highpass-filtered turbulent heat fluxes).
596

597 There is a positive association of the highpass-filtered THF with the OEI in positive regression,
598 such that as the OEI becomes more positive, the heat flux variability increases just downstream
599 of the OE region (180-160°W,40°N) and to the south of the OE front (Figure 8e). The heat flux
600 variability reflects the passage of the warm and cold sectors of a low-pressure system over the
601 ocean; fluxes are upwards (positive) in the cold sector and downwards (negative) in the warm
602 sector. Increased variability reflects an increased frequency of large positive and negative

values, which indicates increased storm-track activity as the OEI becomes more positive and the front shifts northwards.

The regressions using the FDI show similar asymmetry to those based on the OEI. Meridional wind shows a higher level of significance, and significance is more widespread for EGR (Figure 9b, Table 3). Significance for omega at 500hPa are shifted southwards relative to those for the OEI (Figure 9a). An increase in SST front disturbance from climatology is associated with a low-pressure monopole a month later, with increased storm-track activity to the south of the monopole.

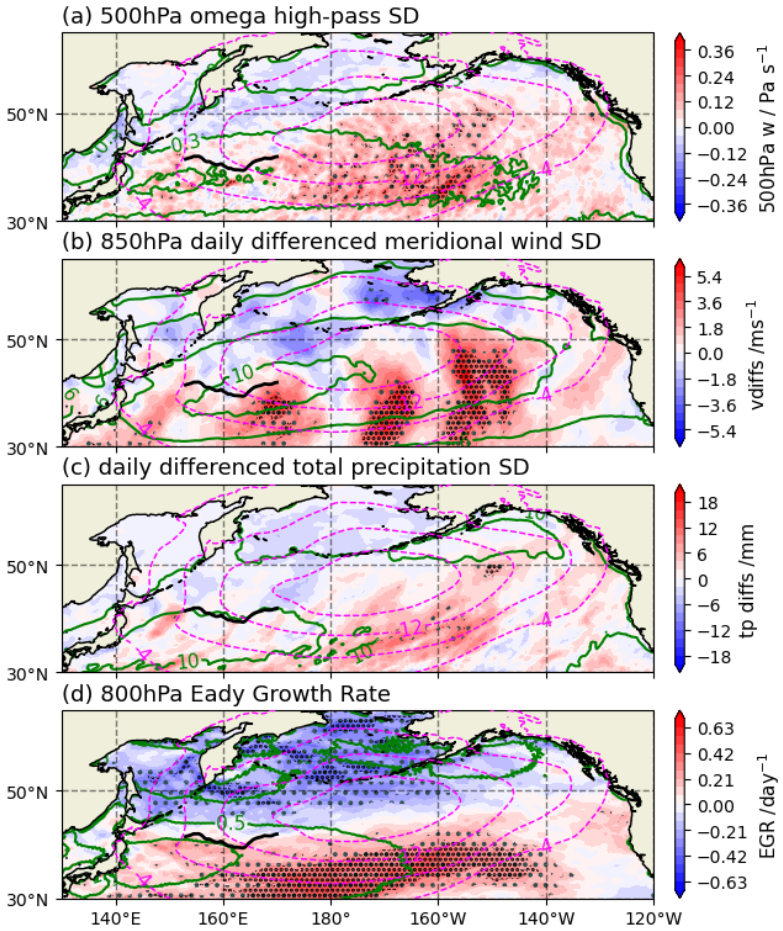

Figure 9. As for Figure 8, except for regression on the average FDI, 155-164°E for positive regressions. SLP contours are 4hPa. Note the colorbar scales are different from those in Figure 8.

Significant negative regressions are found when precipitation differences and omega (Table 3a) are regressed onto the mean FDI, but not for any of the individual datasets. These are not shown in Figure 9, but are located upstream over the Sea of Okhotsk. There is also higher

agreement in the THF regression field between datasets for the FDI compared with OEI (Table 3) although this is not reflected in the mean index.

A notable aspect of these results is that the spatial patterns of significant regression coefficients for the OEI and FDI in positive regression are very similar (Figures 8a-d and Figure 9), as discussed in section 4.3. Specifically, the positive phases of the FDI and OEI are significantly positively correlated (r=0.52-0.59), which suggests that the atmospheric response to each time series in this phase would show similarities. Both indices project onto a pressure monopole near the Aleutians (thin magenta lines show SLP in Figures 8 and 9). For the OEI, this indicates a deepening of the climatological low pressure centered over the Aleutians, enhancing the storm-track activity to the south. For the FDI, the monopole is shifted about 10° further south, representing a southward displacement of the climatological low pressure. However, significant storm-track metric responses are at very similar locations, on the southern flank of this monopole. This indicates a strengthening and eastward extension of the climatological storm-track steered by the enhanced poleward low-pressure region, as seen by comparing with the location of the climatological values of the metrics (green contours). However, the associated SST front changes associated with the very similar atmospheric responses are different: for the OEI, it is a northward (southward) shift that increases (decreases) storm track activity when the OE is in the positive phase (recall that the mean is subtracted in asymmetric regressions). For the FDI, it is increased (decreased) disturbance from the mean, when the FDI is already in the positive (increased displacement) phase, that is associated with the increased (decreased) storm track variability. As seen in section 4.4, the FDI is an indicator of ocean mesoscale eddy variability, so an increase in mesoscale eddy activity polewards of 40°N in the central OE region is associated with increased storm-track activity.

To summarise the regression patterns for the FDI, in positive regressions (when the central OE has an SST front displaced from the mean), changes in frontal disturbance have a significant association with atmospheric variability (Table 3, Figure 9), indicating a downstream extension or contraction of the storm-track as the positive FDI decreases or increases.

5. Discussion and Summary

We have shown that the OEI and subsequent regressions with atmospheric fields are dataset dependent. Dataset selection is therefore an important aspect of a study's design and we would recommend considering more than one dataset, along with using different metrics for

quantifying the SST fronts, to identify the robust features of air-sea interactions. SSTs used in ERA5 in particular appear to be an outlier, showing weaker correlations with indices from other datasets, and markedly different responses in regression maps. On average, ERA5 underestimates the SST variability in the KE region compared with an ensemble median of SST datasets (Yang et al., 2021). These WBC regions have higher mesoscale eddy activity, and it is possible that the SSTs used in ERA5 underestimate the SST fluctuations in this region (Sroka et al., 2022). Calculating the amplitude of the SST mesoscale eddy activity for ERA5, as for Figure 7a, confirms this (not shown).

We have found that the storm-track related air-sea interactions associated with the OE have a significant asymmetric component. The fact that the positive regression phase for OEI and FDI show very similar regression patterns (even closer than some OEI regression patterns from different datasets) is noteworthy, and the timeseries show moderate positive correlations in the positive phase. Both the northward shift of the OE in its positive phase, and the increasing shift away from climatology for the FDI, are associated with increased downstream storm-track activity and a monopole of low pressure near the Aleutian Islands. Another striking feature of the FDI is that although correlations between the indices of the different datasets are no better than those of the OEI, there is much more agreement between the regressions of the FDI from different datasets.

The FDI is a novel index designed to quantify the disruption of the maximum SST gradient in the central section of the OE. Increased mesoscale eddy activity in the SST field to the north acts against the mean poleward SST gradient and the local SST gradient maximum at around 40°N, resulting in a disrupted maximum SST gradient and an increased FDI. The increased mesoscale eddy activity and increased FDI are associated with increased storm-track activity. This is consistent with previous model results (Ma et al., 2017; Jia et al., 2020) where atmospheric baroclinic growth is modified via the presence of oceanic eddies. This results in increased moisture content in the marine atmospheric boundary layer, and enhanced cyclogenesis via moist baroclinic instability. The origins of this eddy activity have not been determined, and will be left for future research, however there may be links with KE variability and the strength of the Isoguchi jets (Isoguchi et al., 2006; Seo et al., 2014; Sugimoto and Hanawa, 2011; Sugimoto 2014).

687 The northward shift of the OE is easier to understand in the context of storm-tracks being
688 anchored on the northern flanks of SST fronts; high baroclinicity is maintained by the contrast
689 in heat supply across the SST front (e.g. Nakamura et al., 2008), so that shifts in the SST fronts
690 will have an impact on the storm track. Considering the central section of the OE, the
691 displacement of the SST front from climatology as measured by the FDI, has an impact on the
692 storm-track.
693
694 The association of the FDI with mesoscale eddy variability is interesting but cannot be easily
695 explained within the scope of this paper. Eddies can erode the SST front through increased
696 surface heat loss (e.g. Nonaka et al., 2009). However, recent studies indicate that eddies may
697 also act to maintain SST fronts, through vertical heat transport replenishing the heat lost from
698 the surface (Jing et al., 2021). Tang et al. (2022) report that most eddies weaken the SST
699 gradient within the eddies, but induce the redistribution of the SST front in the surrounding
700 ocean, which varies according to whether eddies are cyclonic or anticyclonic.
701
702 The OEI appears to perform poorly as a measure of high-frequency (i.e., storm-track related)
703 air-sea interaction based on using a one-month lag between the OEI and the subsequent storm-
704 track variable and when considering consistency between datasets. Previous research has
705 identified more significant air-sea-interactions than found here due to different research foci.
706 For example, Frankignoul et al. (2011) examine the OEI in the context of large-scale
707 atmospheric variability. Indeed, their results are consistent with those presented here as they
708 find little significance at one month lag but stronger signals at lags of two to five months. In
709 addition, our focus is winter, whereas Frankignoul et al. (20110 find a strong response based
710 on all months as well as with an August-October index and November-January atmospheric
711 fields. The growth in high-frequency weather systems as indicated by the storm-track response
712 may subsequently lead to changes in diabatic heating and momentum and heat fluxes by these
713 high-frequency systems, with subsequent changes in the jetstream. However, in the present
714 study we do not consider the FDI impacts at different lag times which may reveal such
715 responses. Neither do we compare early and late winter differences, or differences at other
716 times in the year. Investigating the physical mechanisms which link fluctuations in the positive
717 FDI to changes in the storm track is also left for future research. Here we simply present the
718 FDI as a complementary approach to identifying high-frequency air-sea interactions, which at
719 short timescales with a lag of around one month, produces more consistent air-sea interaction
720 results when using different datasets to derive the index than does the OEI.

The key findings of the study are summarised below.

1. The OEIs obtained from different datasets show considerable variation. Correlations are stronger on seasonal or bimonthly timescale, but weak on a subseasonal scale. We do not recommend using indices such as the OEI for identifying subseasonal variability in air-sea interactions, due to the large discrepancies between datasets at this temporal scale. Identifying a single *best* dataset to use for defining the OEI is not clearly achievable. However we advise against the use of ERA5 SST data, as it is a clear outlier.
2. These differences arise from slight differences in the representation of SST gradients in the considered datasets, particularly in the more complex central regions where there are parallel fronts or fronts are weak.
3. When used to diagnose air-seas interactions, the OEIs from different SST products can produce different spatial patterns, which may have significant impacts on feature identification and explanations.
4. We develop a new index, the FDI, to quantify the complex central region of the OE, and the extent to which the SST gradient deviates from climatology. This new index is associated with the strength of the SST gradient at 40°N. This gradient is in turn affected by fluctuations in ocean mesoscale eddy activity to the north and south.
5. The FDI has an asymmetric association with air-sea interactions. When the average deviation from climatology is high, a further increase in disturbance is associated with an eastward extension of the storm track. These responses are linked to ocean mesoscale eddy activity in the region.
6. Similarly, the response of storm-track metrics to the north-south shifts of the OE front is asymmetric. It is the positive regression phase that is significant (when the OE front is shifted to the north).
7. The FDI produces a more robust air-sea interaction signal with storm-track metrics than the OEI, for the one-month time lag considered here, as there is more agreement between the regressions based on indices calculated from the different SST datasets and the significance of the regressions is often at a higher threshold. The agreement in the FDI regression results across datasets is notable as the correlations between the FDI from different datasets are actually similar to (or in the case of GMPE, lower than) the correlations between the different OEIs, yet more consistent regression results are obtained.

8. An important feature of the OEI and FDI regressions is that the positive regression phase produces very similar spatial regression patterns. This reflects the fact that when the FDI and OEI are partitioned by OEI phase, positive correlations are found in the positive phase.

Acknowledgements. The authors acknowledge support from the NSFGEO-NERC project 'Large-scale atmospheric circulation response to Oyashio Extension frontal variability', award AGS-2040073. The National Center for Atmospheric Research (NCAR) is a major facility sponsored by the US National Science Foundation (NSF) under Cooperative Agreement No. 1852977.

Data availability statement. All data used in this study are available online.

References.

Banzon, V., T. M. Smith, T. M. Chin, C. Liu, and W. Hankins (2016), A long-term record of blended satellite and in situ sea-surface temperature for climate monitoring, modeling and environmental studies, *Earth Syst. Sci. Data*, *8*(1), 165-176, doi:10.5194/essd-8-165-2016.

Benjamini, Y., and Y. Hochberg (1996), Controlling the false discovery rate: a practical and powerful approach to multiple testing. *Journal of the Royal Statistical Society,57B,*289-300

Czaja, A., C. Frankignoul, S. Minobe, and B. Vannière (2019), Simulating the Midlatitude Atmospheric Circulation: What Might We Gain From High-Resolution Modeling of Air-Sea Interactions?, *Current Climate Change Reports*, *5*(4), 390-406, doi:10.1007/s40641-019-00148-5.

Donlon, C. J., M. Martin, J. Stark, J. Roberts-Jones, E. Fiedler, and W. Wimmer (2012), The Operational Sea Surface Temperature and Sea Ice Analysis (OSTIA) system, *Remote Sensing of Environment*, *116*, 140-158, doi:10.1016/j.rse.2010.10.017.

Fiedler, E. K., and Coauthors, (2019), Intercomparison of long-term sea surface temperature analyses using the GHRSST Multi-Product Ensemble (GMPE) system, *Remote Sensing of Environment*, *222*, 18-33, doi:10.1016/j.rse.2018.12.015.

788 Frankignoul, C., and Y.-O. Kwon (2022), On the Statistical Estimation of Asymmetrical Relationship
789 Between Two Climate Variables, *Geophys. Res. Lett.*, *49*(20), e2022GL100777,
790 doi:https://doi.org/10.1029/2022GL100777.
791
792 Frankignoul, C., N. Sennéchael, Y.-O. Kwon, and M. A. Alexander (2011), Influence of the
793 Meridional Shifts of the Kuroshio and the Oyashio Extensions on the Atmospheric Circulation,
794 *Journal of Climate*, *24*(3), 762-777, doi:10.1175/2010jcli3731.1.
795
796 Good, S., and Coauthors (2020), The Current Configuration of the OSTIA System for Operational
797 Production of Foundation Sea Surface Temperature and Ice Concentration Analyses, *Remote Sensing*,
798 *12*(4), doi:10.3390/rs12040720.
799
800 Hersbach, H., and Coauthors (2020), The ERA5 global reanalysis, *Quarterly Journal of the Royal*
801 *Meteorological Society*, *146*(730), 1999-2049, doi:https://doi.org/10.1002/qj.3803.
802
803 Hoskins, B. J., and P. J. Valdes (1990), On the Existence of Storm-Tracks, *J. Atmos. Sci.*, *47*(15),
804 1854-1864, doi:https://doi.org/10.1175/1520-0469(1990)047<1854:OTEOST>2.0.CO;2.
805
806 Huang, B., C. Liu, E. Freeman, G. Graham, T. Smith, and H.-M. Zhang (2021), Assessment and
807 Intercomparison of NOAA Daily Optimum Interpolation Sea Surface Temperature (DOISST) Version
808 2.1, *Journal of Climate*, *34*(18), 7421-7441, doi:10.1175/jcli-d-21-0001.1.
809
810 Isoguchi, O., H. Kawamura, and E. Oka (2006), Quasi-stationary jets transporting surface warm waters
811 across the transition zone between the subtropical and the subarctic gyres in the North Pacific, *J.*
812 *Geophys. Res.*, *111*(C10), doi:10.1029/2005jc003402.
813
814 Kida, S., and Coauthors (2015), Oceanic fronts and jets around Japan: a review, *Journal of*
815 *Oceanography*, *71*(5), 469-497, doi:10.1007/s10872-015-0283-7.
816
817 Kuwano-Yoshida, A., and S. Minobe (2017), Storm-Track Response to SST Fronts in the
818 Northwestern Pacific Region in an AGCM, *Journal of Climate*, *30*(3), 1081-1102, doi:10.1175/jcli-d-
819 16-0331.1.
820

821 Jia, Y., P. Chang, I. Szunyogh, R. Saravanan, and J. T. Bacmeister (2019), A Modeling Strategy for
822 the Investigation of the Effect of Mesoscale SST Variability on Atmospheric Dynamics, *Geophys. Res.*
823 *Lett.*, *46*(7), 3982-3989, doi:https://doi.org/10.1029/2019GL081960.
824
825 Jing, Z., and Coauthors (2021), Maintenance of mid-latitude oceanic frontsby mesoscale eddies, *Sci.*
826 *Adv.* 6, eaba7880, doi: 10.1126/sciadv.aba7880.
827
828 Kwon, Y.-O., M. A. Alexander, N. A. Bond, C. Frankignoul, H. Nakamura, B. Qiu, and L. A.
829 Thompson (2010), Role of the Gulf Stream and Kuroshio–Oyashio Systems in Large-Scale
830 Atmosphere–Ocean Interaction: A Review, *Journal of Climate*, *23*(12), 3249-3281,
831 doi:10.1175/2010jcli3343.1.
832
833 Ma, X., P. Chang, R. Saravanan, R. Montuoro, H. Nakamura, D. Wu, X. Lin, and L. Wu (2017),
834 Importance of Resolving Kuroshio Front and Eddy Influence in Simulating the North Pacific Storm
835 Track, *Journal of Climate*, *30*(5), 1861-1880, doi:10.1175/jcli-d-16-0154.1.
836
837 Martin, M., and Coauthors (2012), Group for High Resolution Sea Surface temperature (GHRSST)
838 analysis fields inter-comparisons. Part 1: A GHRSST multi-product ensemble (GMPE), *Deep Sea*
839 *Research Part II: Topical Studies in Oceanography*, *77-80*, 21-30, doi:10.1016/j.dsr2.2012.04.013.
840
841 Nakamura, H., T. Sampe, A. Goto, W. Ohfuchi, and S.-P. Xie (2008), On the importance of midlatitude
842 oceanic frontal zones for the mean state and dominant variability in the tropospheric circulation,
843 *Geophys. Res. Lett.*, *35*(15), doi:10.1029/2008gl034010.
844
845 Nonaka, M., H. Nakamura, B. Taguchi, N. Komori, A. Kuwano-Yoshida, and K. Takaya (2009), Air-
846 Sea Heat Exchanges Characteristic of a Prominent Midlatitude Oceanic Front in the South Indian
847 Ocean as Simulated in a High-Resolution Coupled GCM, *Journal of Climate 22*: 6515-6535, doi:
848 10.1175/2009JCLI2960.1
849
850 Qiu, B., S. Chen, and N. Schneider (2017), Dynamical Links between the Decadal Variability of the
851 Oyashio and Kuroshio Extensions, *Journal of Climate*, *30*(23), 9591-9605, doi:10.1175/jcli-d-17-
852 0397.1.
853

854 Qiu, B. (2019), Kuroshio and Oyashio Currents, in *Encyclopedia of Ocean Sciences*, edited, pp. 384-
855 394, doi:10.1016/b978-0-12-409548-9.11295-3.
856
857 Révelard, A., C. Frankignoul, N. Sennéchael, Y.-O. Kwon, and B. Qiu (2016), Influence of the Decadal
858 Variability of the Kuroshio Extension on the Atmospheric Circulation in the Cold Season, *Journal of*
859 *Climate*, *29*(6), 2123-2144, doi:https://doi.org/10.1175/JCLI-D-15-0511.1.
860
861 Révelard, A., C. Frankignoul, and Y.-O. Kwon (2018), A Multivariate Estimate of the Cold Season
862 Atmospheric Response to North Pacific SST Variability, *Journal of Climate*, *31*(7), 2771-2796,
863 doi:10.1175/jcli-d-17-0061.1.
864
865 Reynolds, R. W., T. M. Smith, C. Liu, D. B. Chelton, K. S. Casey, and M. G. Schlax (2007), Daily
866 High-Resolution-Blended Analyses for Sea Surface Temperature, *Journal of Climate*, *20*(22), 5473-
867 5496, doi:https://doi.org/10.1175/2007JCLI1824.1.
868
869 Sampe, T., H. Nakamura, A. Goto, and W. Ohfuchi (2010), Significance of a Midlatitude SST Frontal
870 Zone in the Formation of a Storm Track and an Eddy-Driven Westerly Jet, *Journal of Climate*, *23*(7),
871 1793-1814, doi:10.1175/2009jcli3163.1.
872
873 Seo, Y., S. Sugimoto, and K. Hanawa (2014), Long-Term Variations of the Kuroshio Extension Path
874 in Winter: Meridional Movement and Path State Change, *Journal of Climate*, *27*(15), 5929-5940,
875 doi:https://doi.org/10.1175/JCLI-D-13-00641.1.
876
877 Seo, H., and Coauthors (2023), Ocean Mesoscale and Frontal-Scale Ocean–Atmosphere Interactions
878 and Influence on Large-Scale Climate: A Review, *Journal of Climate*, *36*(7), 1981-2013,
879 doi:10.1175/jcli-d-21-0982.1.
880
881 Small, R. J., R. A. Tomas, and F. O. Bryan (2014), Storm track response to ocean fronts in a global
882 high-resolution climate model, *Climate Dynamics*, *43*(3), 805-828, doi:10.1007/s00382-013-1980-9.
883
884 Small, R. J., R. Msadek, Y.-O. Kwon, J. F. Booth, and C. Zarzycki (2019), Atmosphere surface storm
885 track response to resolved ocean mesoscale in two sets of global climate model experiments, *Climate*
886 *Dynamics*, *52*(3), 2067-2089, doi:10.1007/s00382-018-4237-9.

887
888 Smirnov, D., M. Newman, M. A. Alexander, Y.-O. Kwon, and C. Frankignoul (2015), Investigating
889 the Local Atmospheric Response to a Realistic Shift in the Oyashio Sea Surface Temperature Front,
890 *Journal of Climate*, *28*(3), 1126-1147, doi:https://doi.org/10.1175/JCLI-D-14-00285.1.
891
892 Sroka, S., A. Czaja, and S. Chakravorty (2022), Assessing the importance of mesoscale sea-surface
893 temperature variations for surface turbulent cooling of the Kuroshio Extension in wintertime,
894 *Quarterly Journal of the Royal Meteorological Society*, *148*(747), 2742-2754,
895 doi:https://doi.org/10.1002/qj.4333.
896
897 Sugimoto, S. (2014), Influence of SST Anomalies on Winter Turbulent Heat Fluxes in the Eastern
898 Kuroshio–Oyashio Confluence Region, *Journal of Climate*, *27*(24), 9349-9358, doi:10.1175/jcli-d-14-
899 00195.1.
900
901 Sugimoto, S., and K. Hanawa (2011), Roles of SST Anomalies on the Wintertime Turbulent Heat
902 Fluxes in the Kuroshio–Oyashio Confluence Region: Influences of Warm Eddies Detached from the
903 Kuroshio Extension, *Journal of Climate*, *24*(24), 6551-6561,
904 doi:https://doi.org/10.1175/2011JCLI4023.1.
905
906 Taguchi, B., H. Nakamura, M. Nonaka, N. Komori, A. Kuwano-Yoshida, K. Takaya, and A. Goto
907 (2012), Seasonal Evolutions of Atmospheric Response to Decadal SST Anomalies in the North Pacific
908 Subarctic Frontal Zone: Observations and a Coupled Model Simulation, *Journal of Climate*, *25*(1),
909 111-139, doi:https://doi.org/10.1175/JCLI-D-11-00046.1.
910
911 Tang, R., Y. Yu., J. Xi, W. Ma, and Y. Wang (2022), Mesoscale Eddies Induce Variability in
912 the Sea Surface Temperature Gradient in the Kuroshio Extension, *Front. Mar. Sci.* 9:926954,
913 doi: 10.3389/fmars.2022.926954.
914
915 Wagawa, T., S.-I. Ito, Y. Shimizu, S. Kakehi, and D. Ambe (2014), Currents Associated with the
916 Quasi-Stationary Jet Separated from the Kuroshio Extension, *Journal of Physical Oceanography*,
917 *44*(6), 1636-1653, doi:https://doi.org/10.1175/JPO-D-12-0192.1.
918

Wallace, J. M., G.-H. Lim, and M. L. Blackmon (1988), Relationship between Cyclone Tracks, Anticyclone Tracks and Baroclinic Waveguides, *J. Atmos. Sci.*, *45*(3), 439-462, doi:https://doi.org/10.1175/1520-0469(1988)045<0439:RBCTAT>2.0.CO;2.

Wilks, D. S. (2016), "The Stippling Shows Statistically Significant Grid Points": How Research Results are Routinely Overstated and Overinterpreted, and What to Do about It, *Bulletin of the American Meteorological Society*, *97*(12), 2263-2273, doi:https://doi.org/10.1175/BAMS-D-15-00267.1.

Wills, S. M., and D. W. J. Thompson (2018), On the Observed Relationships between Wintertime Variability in Kuroshio–Oyashio Extension Sea Surface Temperatures and the Atmospheric Circulation over the North Pacific, *Journal of Climate*, *31*(12), 4669-4681, doi:10.1175/jcli-d-17-0343.1.

Wu, B., X. Lin, and B. Qiu (2018), Meridional Shift of the Oyashio Extension Front in the Past 36 Years, *Geophys. Res. Lett.*, *45*(17), 9042-9048, doi:https://doi.org/10.1029/2018GL078433.

Yang, C., et al. (2021), Sea Surface Temperature Intercomparison in the Framework of the Copernicus Climate Change Service (C3S), *Journal of Climate*, *34*(13), 5257-5283, doi:10.1175/jcli-d-20-0793.1.

Yao, Y., Z. Zhong and X-Q. Yang (2018a), Influence of the subarctic front intensity on the midwinter suppression of the North Pacific storm track, *Dynamics of Atmospheres and Oceans,* 81, 63-72, doi:10.1016/j.dynatmoce.2018.01.001.

Yao, Y., Z. Zhong, X-Q. Yang and X Huang (2018b), Seasonal variation of the North Pacific storm-track relationship with the Subarctic frontal zone intensity, *Dynamics of Atmospheres and Oceans*, 83, 75-82, doi: 10.1016/j.dynatmoce.2018.06.003.

Yasuda, I. (2003). Hydrographic structure and variability in the Kuroshio-Oyashio transition area. *Journal of Oceanography* 59, 389-402.

Yook, S., D. W. J. Thompson, L. Sun, and C. Patrizio (2022), The Simulated Atmospheric Response to Western North Pacific Sea Surface Temperature Anomalies, *Journal of Climate*, *35*(11), 3335-3352, doi:10.1175/jcli-d-21-0371.1.